PHYSICAL REVIEW B **84**, 195135 (2011)

High-resolution x-ray absorption spectroscopy of $BaTiO_3$: Experiment and first-principles calculations

A. Chassé, St. Borek, K.-M. Schindler, M. Trautmann, M. Huth, and F. Steudel
Institute of Physics, Martin-Luther-University Halle–Wittenberg, DE-06099 Halle, Germany

L. Makhova, J. Gräfe, and R. Denecke
Wilhelm-Ostwald Institute of Physical and Theoretical Chemistry, University Leipzig, DE-04103 Leipzig, Germany

(Received 15 July 2011; revised manuscript received 29 September 2011; published 28 November 2011)

High resolution x-ray absorption spectroscopy (XAS) affords new insight into the microscopic properties of perovskite transition metal oxides. Interpretation of XAS spectra in transition metal oxides requires theoretical tools capable of describing relativistic and many-body effects. In this work, full relativistic (SPR-KKR) and multiplet calculations (CTM4XAS) are carried out and compared to experimental multiedge XAS spectra of $BaTiO_3$ single crystals. The impact of relativistic and many-body effects on the calculated density of states and x-ray absorption near edge structure spectra are individually considered.

DOI: 10.1103/PhysRevB.84.195135 PACS number(s): 71.15.Mb, 11.80.La, 71.20.−b, 77.84.Cg

I. INTRODUCTION

$BaTiO_3$ (BTO) is considered to be a promising candidate ferroelectric material for magnetoelectric composites and layered film structures.[1] BTO, a perovskite material, has been intensively investigated over the last half century. With the increasing affordability of computation and advancement of theoretical tools in the 1990s, the theoretical description of electronic, structural, and dynamical properties became an area of active research. The development of first-principles techniques based on density functional theory (DFT) within the local density approximation (LDA) inspired fundamental investigations of ferroelectricity and related phenomena. These *ab initio* methods remain the foremost tools by which atomic-scale phenomena in ferroelectric oxides can be studied.[2]

X-ray absorption spectroscopy (XAS) constitutes the state-of-the-art method to investigate simultaneously the electronic, structural, and magnetic properties of perovskite-like or multiferroic systems. The method sheds light on complex systems' atomic environment, chemical state, and local magnetic information.[3,4] There has been great progress in the calculations and interpretations of x-ray absorption spectra over the past decade. DFT-LDA methods constitute here the state-of-the-art theory. However, the method is restricted to zero temperature and does not adequately describe excited state phenomena. Excited states and phase transitions that occur at nonzero temperatures, however, must be considered in order to interpret BTO XAS data. Within one-electron DFT-LDA, different corrections simulate both the many-body character of electronic excitations and experimental conditions. These corrections include the electron-core hole interaction, screening of the x-ray field, inelastic losses, and temperature effects.[5]

In this paper, x-ray absorption measurements and calculations are presented for several x-ray absorption edges in BTO single crystals: O K edge, Ti $L_{2,3}$ edges, and Ba $M_{4,5}$ edges. These measurements' high resolution ($\Delta E \leqslant 0.2$ eV) allows comparison of theoretical calculations incorporating nonrelativistic (scalar-relativistic) vs. relativistic and one-electron vs. many-electron approximations.

Here we apply a fully relativistic *ab initio* method for the calculation of the site- and l-projected density of states (DOS) for the cubic and tetragonal phases of BTO. The fully relativistic results are compared to nonrelativistic calculations. X-ray absorption spectra were calculated for BTO in the tetragonal phase and compared to high-resolution experimental results. Finally, many-body effects in x-ray absorption spectra were added using atomic multiplet theory, where solid state effects are described with different crystal field parameters.[6] High-resolution measurements allow the identification of various structures and small many-electron contributions with high accuracy.

The paper is organized as follows: Sec. II discusses experimental details and results. Section III introduces the Green's function theory of x-ray absorption spectroscopy and different approximations. Then, experimental and theoretical results for O K, Ti $L_{2,3}$, and Ba $M_{4,5}$ absorption edges in BTO single crystals are compared and discussed in Sec. IV. Finally, a short summary and outlook are given in Sec. V.

II. EXPERIMENT

The high-resolution XAS experiments were performed in a UHV chamber with a base pressure below 1×10^{-10} mbar. The BTO(001) single crystals were cleaned by heating the sample for 10 min at 650 °C in an oxygen atmosphere of 1.3×10^{-6} mbar and annealing at 700 °C in vacuum for 20 min. Cleanliness of the sample, especially avoidance of carbon contamination, was checked using Auger electron spectroscopy. X-ray absorption spectra were recorded using the high-energy beamline UE56/2 PGM-2 (energy range: 100–1000 eV) of the Synchrotron Radiation Source at BESSY in Berlin.[7] Using the exit slit width (40 μm) and the published calculated resolution data[7] we estimate a resolution of about 150 meV at the Ti L and O K edges and of about 200 meV at the Ba M edge.

All spectra were measured at room temperature. Linear polarizations of the x rays were selected through undulator settings. The angle of light incidence was set using a sample stage with two-axis rotation (azimuthal and polar). All

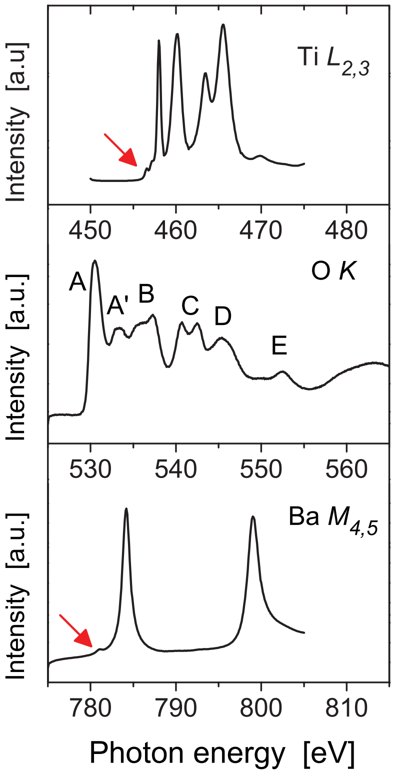

FIG. 1. (Color online) Measured high-resolution x-ray absorption spectra of Ti $L_{2,3}$, O K, and Ba $M_{4,5}$ edges in BTO(001) single crystals at room temperature.

x-ray absorption spectra were recorded in total electron yield measurement mode and normalized to the incident x-ray flux using the drain current from the last refocusing mirror of the beamline.

Figure 1 shows the normalized x-ray absorption spectra at the energies of Ba $M_{4,5}$, Ti $L_{2,3}$, and O K edges. The high-resolution experiment allows detailed insight into fine structures concerning local structure and many-electron effects, which we explain in connection with our first-principles calculations in Sec. IV.

III. GREEN'S FUNCTION THEORY

A. Fermi's Golden Rule

The x-ray absorption coefficient $\mu(\omega)$ can be calculated using Fermi's Golden Rule[3]

$$\mu(\omega) \propto \sum_{\substack{i\ \mathrm{occ} \\ f\ \mathrm{unocc}}} |\langle \Psi_f |\, X_q \,| \Psi_i \rangle|^2 \,\delta(E_f - E_i - \hbar\omega), \tag{1}$$

where the wave functions Ψ_i (energy E_i) and Ψ_f (energy E_f) refer to the initial and final states of the many-electron system. The operator X_q in (1) couples the system to the x-ray photon field [energy $\hbar\omega$, polarization $q \equiv (\mathbf{q},\lambda)$] usually taken in the dipole approximation. The Dirac δ function ensures energy conservation $E_f = E_i + \hbar\omega$.

The Green's function formalism provides an alternate formulation of Fermi's Golden Rule [Eq. (1)]. Using the Dirac identity $\lim_{\eta\to 0} \mathrm{Im}\,(E - E' + i\eta)^{-1} = -\pi\,\delta(E - E')$, we get

$$\mu(\omega) \propto \sum_{i\ occ} \langle \Psi_i | X_q^\dagger \,\mathrm{Im}\, G^+(E_i + \hbar\omega)\, X_q \,| \Psi_i \rangle \times \theta(E_i + \hbar\omega - E_F) \tag{2}$$

with the retarded Green's function

$$G^+(E) = \sum_f \frac{|\Psi_f\rangle\,\langle \Psi_f|}{E - E_f + i\eta}\,. \tag{3}$$

The Heaviside step function $\theta(x)$ in Eq. (2) ensures that the final energy $E = E_i + \hbar\omega$ lies above the Fermi energy E_F.

The Green's function $G^+(E)$ in Eq. (2) can be calculated by means other than the definition Eq. (3). Multiple-scattering theory provides one such method. The Korringa-Kohn-Rostoker (KKR) method[8] expresses $G^+(E)$ in the spatial representation for real energy E by

$$\mathrm{Im}\, G^+(\mathbf{r},\mathbf{r}';E) = \sum_{\Lambda\Lambda'} Z_\Lambda(\mathbf{r},E)\,\mathrm{Im}\,\tau^{00}_{\Lambda\Lambda'}\, Z^\times_{\Lambda'}(\mathbf{r}',E). \tag{4}$$

$\tau^{nm}_{\Lambda\Lambda'}(E)$ is the so-called scattering path operator, where n and m stand for different scattering muffin-tin (MT) centers. Equation (4) requires $n = m = 0$ (position of absorber) because the initial states are well-localized core states of the absorbing atom. Therefore, $\mathbf{r}$ and $\mathbf{r}'$ are in the same MT sphere. In the full relativistic theory, the index $\Lambda = (\kappa, m_j)$ depends on the spin-orbit (κ) and magnetic (m_j) quantum numbers. Z_Λ is the regular solution of the Dirac equation for a spin-dependent potential.[9]

Substituting the KKR Green's function [Eq. (4)] into Fermi's Golden Rule [Eq. (2)] results in

$$\mu(E) \propto \sum_{\Lambda\Lambda'} m^\times_\Lambda(E)\,\mathrm{Im}\,\tau^{00}_{\Lambda\Lambda'}(E)\, m_{\Lambda'}(E)\,\theta(E - E_F), \tag{5}$$

where the matrix element $m_\Lambda = \langle Z_\Lambda | X_q | \psi_i \rangle$ in (5) enforces dipole selection rules.

Unfortunately, the methods based on ground-state properties and the one-electron approximation are restricted in the application of $\mu(E)$ calculations. The final state $|\Psi_f\rangle$ in (1) contains not only an electron in the final state f but also a core hole in the excited core state. Both the excited electron and the core hole decay and interact. Whereas the core hole tends to be filled quite rapidly by Auger transitions, the high-energy electron can excite electron-hole pairs, plasmons, and so on, in inelastic collisions.

For comparison with experimental spectra, we consider the broadened spectra[10]

$$\mu(E) = \frac{1}{2\pi} \int_{E' \geqslant E_F} dE' \,\frac{\Gamma(E')}{(E - E')^2 + \Gamma^2(E')/4}\, \mu_0(E'), \tag{6}$$

where $\mu_0(E)$ is the original one-particle spectrum. The lower limit of the integral E_F is the edge threshold. The energy dependent width $\Gamma(E) = \Gamma_c + \Gamma_x(E)$ in the Lorentzian broadening function depends on the core hole width Γ_c and the width of the excited band energy. In addition, a commonly used

Gaussian broadening has to be taken into account to include finite experimental resolution.

B. Calculation of τ matrix

For an infinite and periodic array of atoms, the τ matrix is calculated by means of lattice Fourier transformation. This approach leads to[9]

$$\tau^{00}_{\Lambda\Lambda'}(E) = \frac{1}{\Omega_{\mathrm{BZ}}} \int_{\mathrm{BZ}} d^3\mathbf{k}\,[t^{-1}(E) - G_0(\boldsymbol{k},E)]^{-1}_{\Lambda\Lambda'}, \qquad (7)$$

where the $\mathbf{k}$ integral runs over the first Brillouin zone (BZ). The quantity $G_0(\mathbf{k},E)$ in Eq. (7) is called the KKR structure constants matrix and the expression $[\cdots]$ in Eq. (7) is the so-called KKR matrix $[M(\mathbf{k},E)]$. Symmetry relations allow the reduction of the integration region Ω_{BZ} to a wedge. For the treatment of spin-orbit and magnetic effects the relativistic generalization is important as realized in Ebert's spin-polarized relativistic KKR (SPR-KKR) code[11,12] with several new extensions.[13–15]

Recently, a real space Green's function (RSGF) approach for a finite array of atoms (cluster approximation) was presented in which the multiple-scattering expansion is carried out to all orders (full MS) by matrix inversion[16,17]

$$\underline{\underline{\tau}}(E) = [\underline{\underline{t}}^{-1}(E) - \underline{\underline{G}}_0(E)]^{-1}. \qquad (8)$$

Real space multiple scattering calculations can be improved by taking into account the influence of the core hole and a fast computation of electron multiple scattering (Lanczos algorithms).[18,19]

C. Relation to DOS

The energy dependence of $\mu(E)$ is related to the unoccupied electronic states of the system. The local density of states (DOS) is defined to be

$$n^0(E) = -\frac{2}{\pi} \int_{\mathrm{cell}} d^3\boldsymbol{r}\,\mathrm{Im}\,G^+(\boldsymbol{r},\boldsymbol{r},E), \qquad (9)$$

where the $\mathbf{r}$ integral runs over the cell occupied by the atom at the origin. The local DOS can be transformed to an angular momentum representation (l-DOS) via

$$n^0(E) = \sum_l \left[\sum_m n^0_L(E) \right] \qquad (10)$$

with

$$n^0_L = -\frac{2}{\pi}\,\mathrm{Im}\,\tau^{00}_{LL}(E) \int_{\mathrm{cell}} dr\, 4\pi\, r^2\, [Z_l(r,E)]^2 \qquad (11)$$

and $L \equiv (l,m)$.

Now we may write the x-ray absorption transition rate in the form[3]

$$\mu(E) \propto \sum_L |\tilde{m}_L(E)|^2\, n^0_L(E) \qquad (12)$$

with the matrix element $\tilde{m}_L(E) = \langle \tilde{Z}_l\, Y_L |\, X_q\, |\psi_c\rangle$. The matrix elements usually vary smoothly and slowly with energy E. Thus the energy dependence of $\mu(E)$ mainly reflects the local density of unoccupied states. The wave function $\tilde{Z}^0_l$ is the radial wave function normalized to unity within the atomic cell. In the case of cubic symmetric crystals, $\tau^{00}_{LL'}$ is diagonal in L up to $l = 2$.

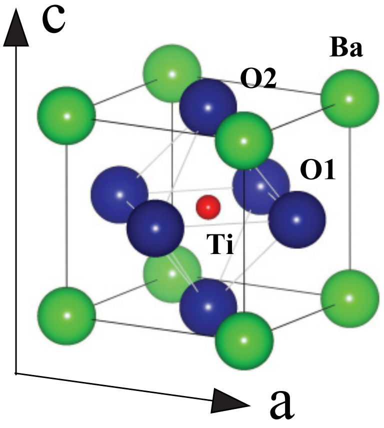

FIG. 2. (Color online) Unit cell of cubic BaTiO$_3$.

IV. RESULTS AND DISCUSSION

A. BTO single crystal structure

BTO undergoes phase transitions from rhombohedral to orthorhombic at 183 K, to tetragonal at 278 K, and to cubic at 393 K. The cubic phase is paraelectric and the other phases are ferroelectric. Here we consider the cubic and tetragonal phases of BTO.

In the Hermann-Mauguin classification, the cubic phase of BTO belongs to the space group $Pm3m$ and shows inversion symmetry. At the Curie temperature of 393 K, a transition to the tetragonal phase ($P4mm$ space group) occurs. The shifts in the atomic positions of oxygen and titanium break the inversion symmetry, inducing a macroscopic polarization, and thus the ferroelectric behavior. Figure 2 shows the unit cell of cubic BTO.

In Table I the atomic positions and structural parameters of the cubic phase and the tetragonal phase are given. The lattice constant $a = 4.01$ Å in cubic BTO is used in order to compare our calculated DOS with previously published results. Different sets of structural parameters are considered in the simulation of our experimental x-ray absorption spectra. The data of Megaw[20] and Kwei *et al.*[21] (see Table I) act here as typical examples for different published data sets.[2]

B. SPR-KKR calculations of DOS

Full relativistic calculations are performed using Lloyd's[22] formula (to improve Fermi energy E_F) and the exchange-correlation potential from Vosko *et al.*[23] Use of other functionals had limited influence on on the calculation.

We use the special point sampling method[24] for BZ integration with 600 k points and angular momentum expansion up to $l_{\max} = 3$ for each atom type in all calculations. The parameters which determine the calculation of the KKR structure constants matrix are the Ewald parameter and the convergence radii in real and reciprocal space,[25] which are $0.8a$, $2.0a$, and $4.0a$, respectively.

TABLE I. Atomic positions and structural parameters of BTO in the cubic and tetragonal phase. Δz denotes the displacement of atoms along the c axis taken from two different experiments (Megaw[20] and Kwei *et al.*[21]).

	Cubic BTO	Tetragonal BTO	
	(x,y,z) $[a]$	Δz $[c]$[20]	Δz $[c]$[21]
Ba	(0.0, 0.0, 0.0)	0.0	0.0
Ti	(0.5, 0.5, 0.5)	0.014	0.0224
O1	(0.5, 0.0, 0.5)	−0.012	−0.0105
O2	(0.5, 0.5, 0.0)	−0.025	−0.0244
a (Å)	4.01	3.9945	3.991
c (Å)		4.0335	4.0352
c/a		1.01	1.01

The calculated band gaps for BTO were 1.8 and 2.1 eV for cubic and tetragonal structures, respectively. These band gaps agree with other *ab initio* methods, but are smaller than the experimental value of 3.2 eV (cubic phase[26]). To get the correct value of the band gap we have to improve the treatment of electronic correlation effects like in hybrid functional or GW methods.[2]

Figure 3 shows the calculated total DOS of BTO in the cubic phase ($a = 4.01$ Å) within a nonrelativistic (left) and a fully relativistic (right) calculation. Besides the total DOS the l-projected DOS for each atom type in the BTO unit cell is given.

The lowest band (O $2s$) is located around −16 eV, in good agreement with experimental data.[27] The Ba $5p$ states lie near −8.5 eV in the nonrelativistic and −10 eV in the relativistic calculation, and are split in the relativistic calculation (see arrows) due to spin-orbit coupling. These states are weakly hybridized with O s and p states. The valence band (VB) edge lies −4.7 eV below the Fermi level (experimental width 6 eV), and is dominated by O $2p$ states that are strongly hybridized with Ti $3d$ states. The band gap appears between the O $2p$ VB and the Ti $3d$ conduction band. The bottom of the empty conduction band arises from the threefold degenerate Ti t_{2g} states, which are lower in energy than the twofold degenerate Ti e_g states (in cubic phase). The edges of bands near the Fermi energy are quite sharp. In the higher energy regions (6–12 eV), the bands are predominantly formed by Ba $5s$ and $5d$ states partially overlapped with Ti e_g states. The conduction band above 14 eV is mainly composed of Ti $4s$ and $4p$ states.

The main differences between the nonrelativistic and relativistic calculations are the energetic position of deep core levels and the Ba $5p$ level, which may influence the calculation of x-ray absorption spectra. In this way, the relation between the experimental energy scale (often the absorption spectrum is recorded in dependence on the photon energy) and the theoretical one (related to the Fermi energy) has to be considered.

In Fig. 4 the calculated nonrelativistic (left) and relativistic (right) total DOS and l-projected DOS of tetragonal BTO of each atomic species are shown. The differences between the cubic (Fig. 3) and the tetragonal phase (Fig. 4) primarily occur due to the change of Ti-O distances and, therefore, the hybridization between Ti $3d$ and O $2p$ states.

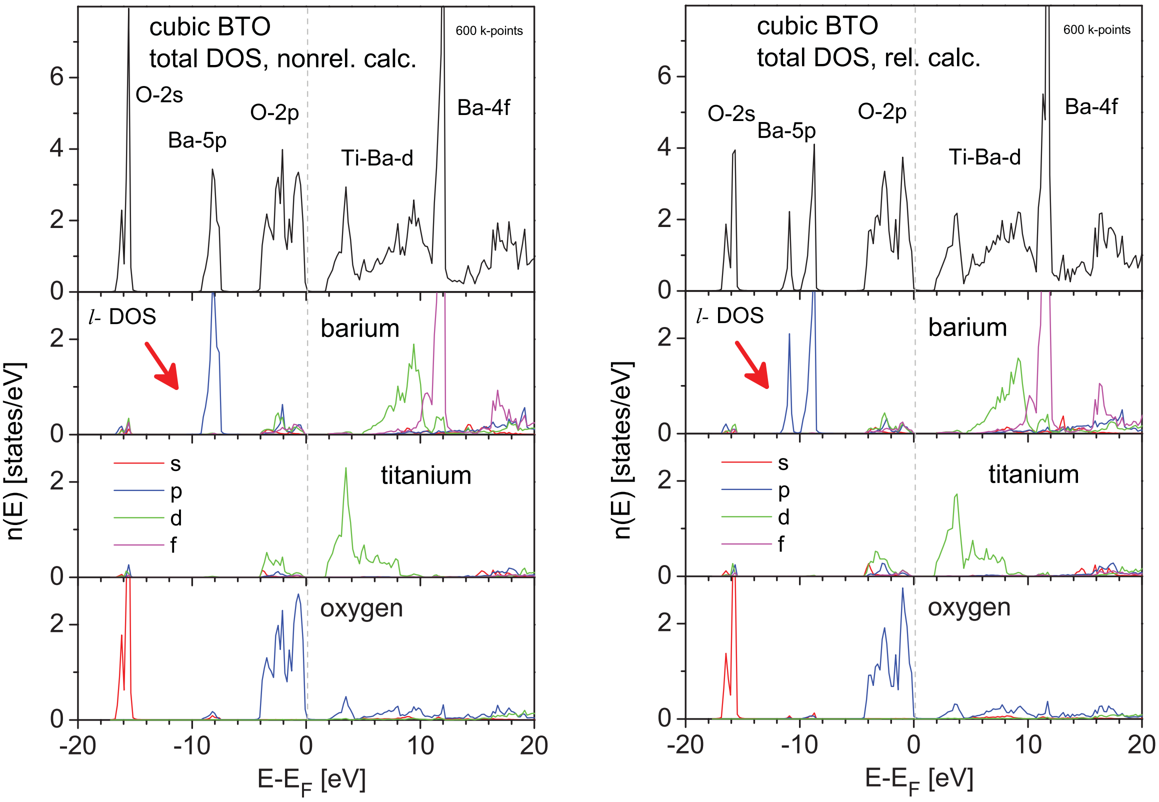

FIG. 3. (Color online) Total and l-projected DOS of cubic BTO ($a = 4.01$ Å): nonrelativistic (left) vs. relativistic (right) calculation.

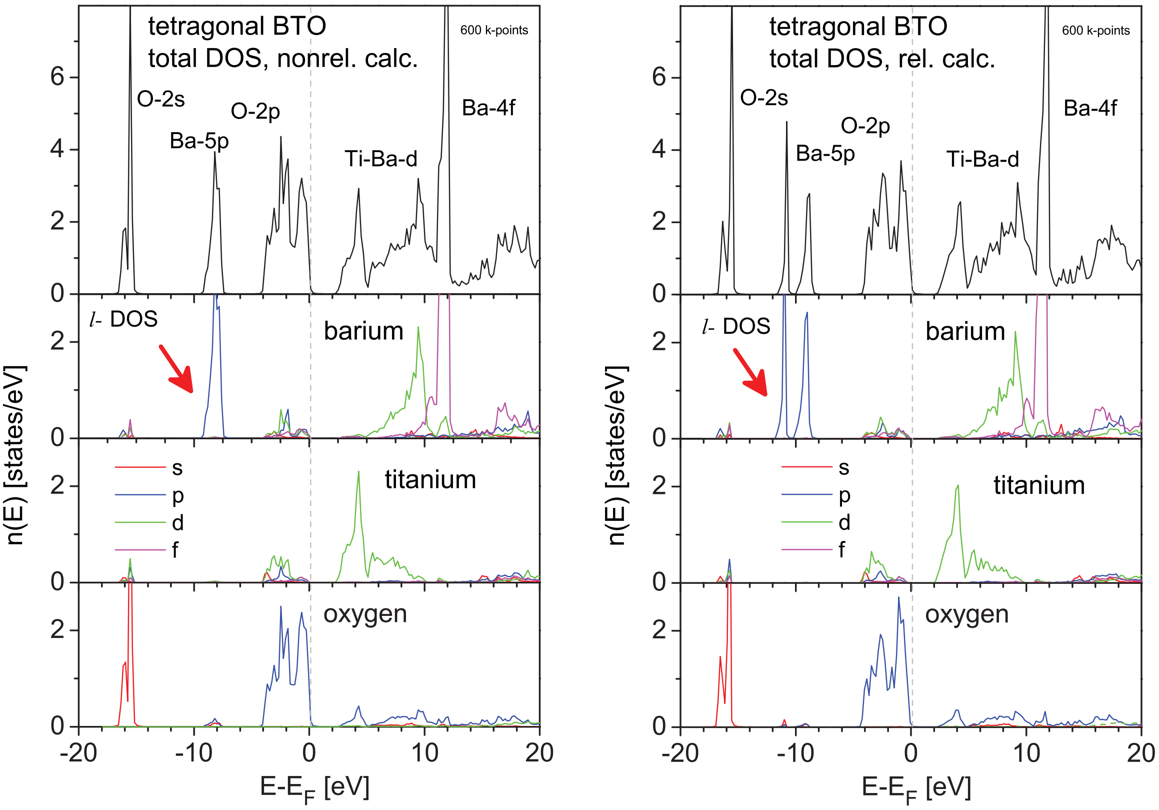

FIG. 4. (Color online) Total and l-projected DOS of tetragonal BTO (structure of Kwei *et al.*[21]): nonrelativistic (left) vs. relativistic (right) calculation.

Figure 5 shows the calculated DOS of Ti $3d$ states in cubic and tetragonal BTO. We have separated the single m contributions to relate parts of the d-DOS of titanium to t_{2g} and e_g states in the cubic (lower part) and the tetragonal (upper part) phase, respectively. The parts for $m = -2, -1, 1$ and for $m = 0, 2$ represent the contributions of d_{xy}, d_{xz}, d_{yz} and d_{z^2}, $d_{x^2-y^2}$ states, respectively, which are related to t_{2g} and e_g in cubic symmetry. The degeneracy is partly lifted in the tetragonal phase.

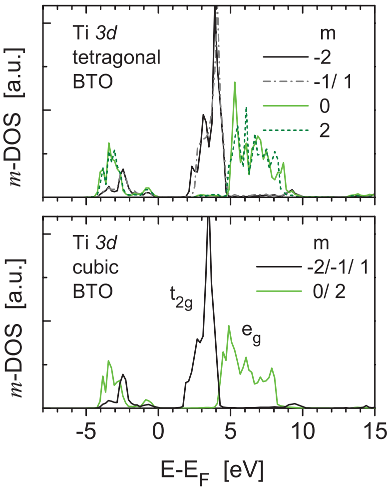

FIG. 5. (Color online) m-projected l-DOS of Ti $3d$ states in tetragonal (upper part) and cubic (lower part) BTO.

Recently, *ab initio* DFT calculations within the generalized gradient approximation (GGA) were presented for both cubic and tetragonal BTO.[28] As in our case, only small differences were found between the considered phases of BTO. The l-projected DOS of O $2p$, Ti $3d$, and Ba $4d$ states are in very good agreement with our calculations. Unfortunately, the behavior of Ba $4f$ states was not shown. Salehi *et al.* published electronic structure calculations of tetragonal[29] and cubic BTO,[30] which show the dependence of the band gap on the employed approximations ($E_g = 1.8, \ldots, 1.95$ eV for cubic BTO; $E_g = 2.6$ eV for tetragonal BTO). In the study of optical properties, band-gap values of 1.85 eV (1.78 eV) for tetragonal (cubic) BTO were found.[31] The separation of t_{2g} and e_g states in the Ti $3d$-DOS (Fig. 5) for cubic BTO may be compared with those of Arai *et al.*[32] All these calculations were done using the full-potential linearized augmented-plane-wave (FP-LAPW) method. Self-consistent *ab initio* DFT-LCAO (linear combination of atomic orbitals) calculations[33,34] give the same results of energy splitting in the Ti $3d$ states. Hartree-Fock (HF), DFT using LCAO, and hybrid-exchange functionals are effective methods for calculations of bulk properties and the electronic structure,[35] so long as exchange-correlation functional and basis set are used. These calculation results agree with those presented here.

Neglecting core hole effects, the absorption coefficient can be related to the angular momentum projected density of unoccupied states. Thus, for example, the K-shell excitation energy dependence of the transition rate reflects the local density of unoccupied p-type states of the excited atom. Here

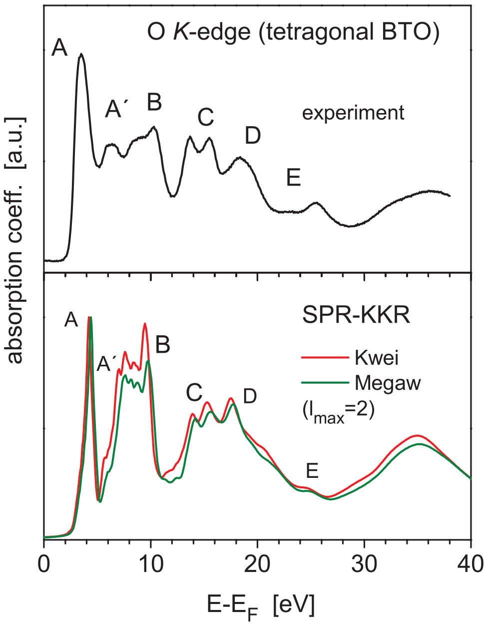

FIG. 6. (Color online) Measured x-ray absorption spectrum of the O K edge (upper part) in comparison to calculated spectra (lower part) for different structural data sets.

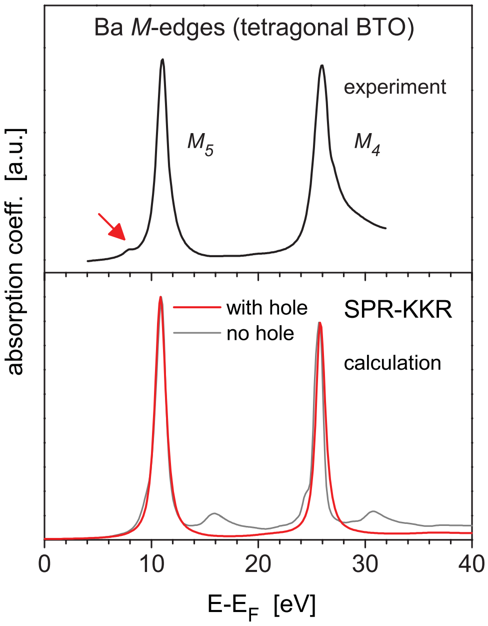

FIG. 7. (Color online) Measured x-ray absorption spectrum of Ba $M_{4,5}$ edges (upper part) in comparison to calculated spectra (lower part).

we have calculated the x-ray absorption coefficient Eq. (1) by means of first-principle calculations using the Green's function methods.

C. O K, Ba $M_{4,5}$, and Ti $L_{2,3}$ edges in BTO

X-ray absorption spectra of the O K, the Ba $M_{4,5}$, and the Ti $L_{2,3}$ edges in single BTO crystals are calculated using the SPR-KKR program package from Ebert's group in Munich.[25] In our SPR-KKR calculations of x-ray absorption spectra, the polarization vector was assigned to be parallel to the crystallographic c axis of the unit cell of BTO, which is also the distortion axis of the tetragonal phase. The spectra are broadened as described, but less broadening was used in the l-projected density of states shown in Fig. 6 to emphasize the different contributions of the unoccupied states. The origin of the energy axis in all calculations is the Fermi energy E_F.

In Fig. 6 the measured x-ray absorption spectrum of the O K edge (upper part) is compared to the calculated x-ray absorption spectra (lower part) with different sets of structural parameters (Kwei vs. Megaw).

The different contributions of the O $1s \rightarrow p$ transition (A–E) can be explained very well by the p-DOS of oxygen and the calculated x-ray absorption spectra. The region up to 7 eV above the O K edge onset corresponds to transitions to final states consisting of O $2p$ character hybridized with TM $3d$ character (features A and A′) with a smaller contribution of O $2p$-Ba $5d$ hybridized states (B). The contribution of t_{2g} is lower in energy than the e_g orbitals of Ti $3d$ states. The separation between A and A′ amounts to 2.1 eV which agrees with the crystal field splitting in the Ti $L_{2,3}$ edges. At 7–20 eV above threshold, the spectra is determined by transitions to final states of mixed O $2p$ and TM $4s$ and $4p$ character as well as Ba p character (features C and D). In experiment and theory, a deep minimum separates the two energy regions at 7–8 eV above the edge.

In comparison to other published results (Refs. 36–40), the agreement between experiment and theory is quite good, even without inclusion of surface effects in our calculations. The choice of structural parameter sets of Megaw and Kwei *et al.* does not affect the agreement between theory and experiment. Only small differences in theoretical spectra occur. The spontaneous polarization of BTO can be simulated by averaging about different directions. This does not change the agreement between experiment and theory. If a single-domain polarized crystal would be available, a linear dichroism (XLD) effect should be observable due to the tetragonal distortion.

The measured and calculated x-ray absorption spectra of the $M_{4,5}$ edges of Ba in BTO single crystals are shown in Fig. 7. The spectra are mainly the result of the dipole-allowed Ba $3d^{10}4f^0 \rightarrow 3d^94f^1$ absorption process. The M_5 and M_4 white lines can be associated with the $3d_{5/2}$ ($\approx$780 eV) and $3d_{3/2}$ ($\approx$795 eV) core hole states, respectively. We can improve the agreement between theoretical and experimental results by taking into account a static core hole in our calculations (Fig. 7). The core hole shifts the unoccupied f states of barium to lower energies which changes the energy dependence of the x-ray absorption spectrum. The small leading peak at 8 eV (arrow in Fig. 7) could not be explained within one-electron theory. However, energy positions and relative intensities of the $M_{4,5}$ edges in relation to other edges may be used as an indicator of chemical or coordination changes in the prepared sample.[41,42]

In contrast to the results of O K and Ba M edges, the measured Ti $L_{2,3}$ edges could not be explained within the one-electron picture. The intensity ratio of $L_3 : L_2$ in the measured spectrum (Fig. 1) is close to 1 : 1, while the one-electron theory predicts an intensity ratio 2 : 1. This discrepancy between

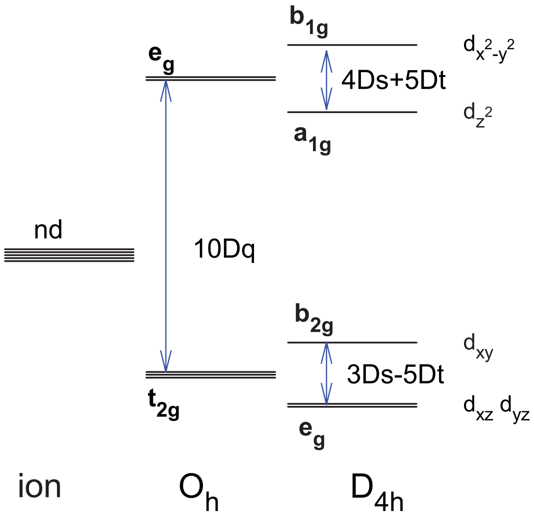

FIG. 8. (Color online) d-level splitting in case of octahedral distortion.

the results of one-electron theories and measurements, well known for 3d TM oxides, may be attributed to the neglected interaction between the photoelectron and the core hole.[4]

D. Multiplet calculations of Ti $L_{2,3}$ edges in BTO

Atomic multiplet calculations, including crystal field effects, are performed for x-ray absorption $L_{2,3}$ edges of titanium in BTO. The approach takes into account many-electron Coulomb and exchange interaction, spin-orbit coupling in initial and final states, and treats the geometrical environment of the absorbing atom in terms of a crystal field potential.[6,43]

In cubic BTO the octahedral surroundings of the Ti^{4+} ion are described by an octahedral crystal field potential which splits the degenerate d states into t_{2g} and e_g states. The strength of the splitting is given by the quantity $10Dq$ (see Fig. 8). The tetragonal distortion of BTO at room temperature reduces the octahedral symmetry (O_h) of the Ti^{4+} ion to D_{4h} symmetry, while the energetic splitting is described by the quantities Dt and Ds (Fig. 8).[44]

All calculations are done within the CTM4XAS package of de Groot.[45] In order to explain the measured Ti $L_{2,3}$ edges of BTO we vary the quantities $10Dq$, Dt, and Ds. The many-electron interactions are taken into account by means of the Slater-Condon integrals F and G, which are reduced by a factor of 0.8.[45] Our investigations show that the exchange contribution (G) of Coulomb repulsion changes the intensity ratio of L_3 and L_2 edge to match experimental ratios.

In Fig. 9 the measured spectrum (upper part) and the calculated spectra (lower part) of the $L_{2,3}$ edges of Ti in cubic (O_h) and tetragonal (D_{4h}) BTO are shown. The calculated spectra are broadened using an energy-dependent broadening for each individual peak. The best agreement between experiment and theory has been found for $10Dq = 1.9$ and $Dt = 0.1$, which is in good agreement with other calculations.[46] Despite the experiment's high resolution (0.15–0.2 eV), broadening effects from the core hole lifetime limit the determination of the tetragonal distortion in BTO from Ti $L_{2,3}$ edges. The small leading peak (Fig. 9) is a typical feature in x-ray absorption spectra of d^0 compounds.[4]

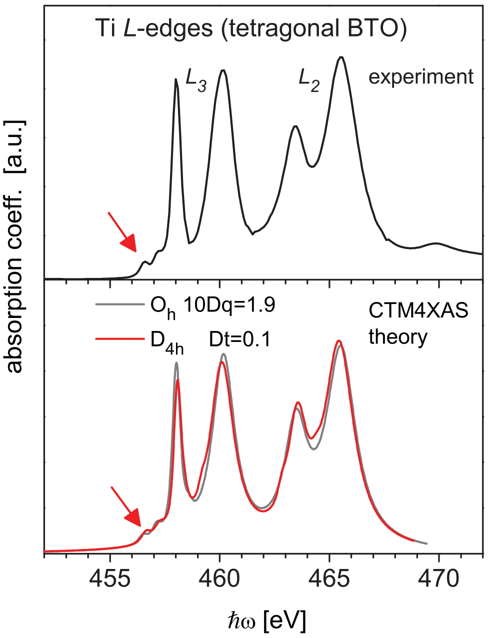

FIG. 9. (Color online) Measured x-ray absorption spectrum of Ti $L_{2,3}$ edges (upper part) and calculated spectra (CTM4XAS) for O_h and D_{4h} symmetry.

It would be interesting to relate the parameters of the crystal field to the energy splitting of Ti 3d states shown in Fig. 5. The two subbands, which we have related to t_{2g} and e_g states are separated by approximately 2 eV (concerning the center of the bands). This value is comparable to the parameter $10Dq$ in the CTM4XAS calculation of cubic BTO. In general, a direct comparison between the 3d-DOS features and the crystal field parameters is not appropriate, as the spacing of energy levels in the crystal field approach results from a many-body interaction.

V. CONCLUSIONS

High resolution x-ray absorption measurements of O K, Ti $L_{2,3}$, and Ba $M_{4,5}$ edges in BTO offer the possibility to support further development of many-electron and core hole interaction theory. Overall, the experimental x-ray absorption spectra of these edges are explained quite well in the framework of SPR-KKR calculations. The one-electron model is successfully applied to interpret O K edge and Ba $M_{4,5}$ edges in BTO. The fine structure in O K spectra are related to individual parts of the calculated l-projected DOS of atoms. Furthermore, the ratio and energetic position of the M_4 and M_5 edges of Ba reflect the bulk properties of BTO. Our calculations of x-ray absorption spectra show minor dependence on small variation of atomic position in bulk tetragonal BTO.

The experimental results of Ti $L_{2,3}$ edges cannot be explained within a one-electron theory. Calculations using multiplet theory take crystal field effects into account, and lend insight on the different contributions of observed intensity ratio and energetic positions of the absorption coefficient. Multiplet parameters $10Dq$, Dt, and Ds control agreement of calculated spectra peak height ratios with experimental results. It appears that the exchange contribution of Coulomb repulsion dominates the many-electron interaction. The $L_{2,3}$ edges of TM ions may be considered as a fingerprint of changes in the local structure of perovskite-like structures and can be used to determine structural parameters in multiferroic systems.

ACKNOWLEDGMENTS

We are grateful for financial support by SFB 762 "Functionality at Oxide Interfaces" (DFG, Germany). The experiments were performed at BESSY (Berlin) with financial support of SFB 762. The authors would like to thank Hubert Ebert's group (Munich) for more than helpful discussions.

---

[1] N. A. Spaldin and M. Fiebig, Science **309**, 391 (2005).

[2] K. Rabe and P. Ghosez, in *Physics of Ferroelectrics: A Modern Perspective*, edited by K. Rabe, C. Ahn, and J.-M. Triscone (Springer, Berlin, 2007).

[3] P. Durham, in *X-ray Absorption (Principles, Applications, Techniques of EXAFS, SEXAFS and XANES)*, edited by D. Koningsberger and R. Prins (John Wiley, New York, 1987).

[4] F. de Groot, Chem. Rev. **101**, 1779 (2001).

[5] J. J. Rehr, J. A. Soininen, and E. L. Shirley, Phys. Scr. T **115**, 207 (2005).

[6] F. de Groot, J. Electron Spectrosc. Relat. Phenom. **61**, 529 (1994).

[7] K. Sawhney, F. Senf, M. Scheer, F. Schäfers, J. Bahrdt, A. Gaupp, and W. Gudat, Nucl. Instrum. Methods A **390**, 395 (1997).

[8] J. Korringa, Physica **13**, 342 (1947); W. Kohn and N. Rostoker, Phys. Rev. **94**, 1111 (1954).

[9] H. Ebert, V. Popescu, and D. Ahlers, Phys. Rev. B **60**, 7156 (1999).

[10] J. E. Müller, O. Jepsen, and J. W. Wilkins, Solid State Commun. **42**, 365 (1982).

[11] H. Ebert, Rep. Prog. Phys. **59**, 1665 (1996).

[12] T. Huhne, C. Zecha, H. Ebert, P. H. Dederichs, and R. Zeller, Phys. Rev. B **58**, 10236 (1998).

[13] J. Schwitalla and H. Ebert, Phys. Rev. Lett. **80**, 4586 (1998).

[14] T. Huhne and H. Ebert, Phys. Status Solidi B **215**, 839 (1999).

[15] J. Minar, L. Chioncel, A. Perlov, H. Ebert, M. I. Katsnelson, and A. I. Lichtenstein, Phys. Rev. B **72**, 045125 (2005).

[16] P. Durham, J. Pendry, and C. Hodges, Comput. Phys. Commun. **25**, 193 (1982).

[17] C. R. Natoli, D. K. Misemer, S. Doniach, and F. W. Kutzler, Phys. Rev. A **22**, 1104 (1980).

[18] A. L. Ankudinov, B. Ravel, J. J. Rehr, and S. D. Conradson, Phys. Rev. B **58**, 7565 (1998).

[19] A. L. Ankudinov, C. E. Bouldin, J. J. Rehr, J. Sims, and H. Hung, Phys. Rev. B **65**, 104107 (2002).

[20] H. Megaw, Acta Crystallogr. **15**, 972 (1962).

[21] G. H. Kwei, A. C. Lawson, S. J. L. Bellinge, and S.-W. Cheong, J. Phys. Chem. **97**, 2368 (1993).

[22] P. Lloyd, Proc. Phys. Soc. **90**, 207 (1972); P. Lloyd and P. V. Smith, Adv. Phys. **21**, 69 (1972).

[23] S. Vosko, L. Wilk, and M. Nusair, Can. J. Phys. **58**, 1200 (1980).

[24] T. Huhne and H. Ebert, Phys. Rev. B **65**, 205125 (2002).

[25] H. Ebert *et al.*, The Munich SPR-KKR package, version 5.4 [http://olymp.cup.uni-muenchen.de/ak/ebert/SPRKKR]; H. Ebert, *Fully Relativistic Band Structure Calculations for Magnetic Solids - Formalism and Application*, in Electronic Structure and Physical Properties of Solids, edited by H. Dreyssé, Lecture Notes in Physics (Springer, Berlin), Vol. 535, p. 191.

[26] S. Wemple, Phys. Rev. B **2**, 2679 (1970).

[27] F. Battye, H. Höchst, and A. Goldmann, Solid State Commun. **19**, 269 (1976).

[28] V. Gallegos-Orozco, R. Martinez-Sanchez, and F. Espinosa-Magana, Phys. Rev. B **77**, 045128 (2008).

[29] H. Salehi, N. Shahtahmasebi, and S. M. Hosseini, Eur. Phys. J. B **32**, 177 (2003).

[30] H. Salehi, S. M. Hosseini, and N. Shahtahmasebi, Chin. J. Phys. **42**, 619 (2004).

[31] G. Gupta, T. Nautiyal, and S. Auluck, Phys. Rev. B **69**, 052101 (2004).

[32] M. Arai, S. Kohiki, H. Yoshikawa, S. Fukushima, Y. Waseda, and M. Oku, Phys. Rev. B **65**, 085101 (2002).

[33] D. D. Bagayoko, G. Zhao, J. Fan, and J. Wang, J. Phys. Condens. Matter **10**, 5645 (1998).

[34] R. Ahuja, O. Ericsson, and B. Johansson, J. Appl. Phys. **90**, 1854 (2001).

[35] S. Piskunov, E. Heifets, R. I. Eglitis, and G. Borstel, Comput. Mater. Sci. **29**, 165 (2004).

[36] Z. Y. Wu, F. Langenhorst, F. Seifert, E. Paris, and A. Marcelli, J. Synchrotron Radiat. **8**, 934 (2001).

[37] L. Soriano, M. Abbate, A. Fernández, A. R. González-Elipe, and J. M. Sanz, Surf. Interface Anal. **25**, 804 (1997).

[38] Y.-H. Tang, M.-H. Tsai, J. C. Jan, and W. F. Pong, Chin. J. Phys. **41**, 167 (2003).

[39] R. Brydson, H. Sauert, W. Engel, and F. Hofer, J. Phys. Condens. Matter **4**, 3429 (1992).

[40] J. Zhang, A. Visinoiu, F. Heyroth, F. Syrowatka, M. Alexe, D. Hesse, and H. S. Leipner, Phys. Rev. B **71**, 064108 (2005).

[41] V. Garcia, M. Bibes, L. Bocher, S. Valencia, F. Kronast, A. Crassous, X. Moya, S. Enouz-Vedrenne, A. Gloter, D. Imhoff, C. Deranlot, N. Mathur, S. Fusil, K. Bouzehouane, and A. Barthélémy, Science **327**, 1106 (2010).

[42] H. Kurata, S. Isojima, M. Kawai, Y. Shimakawa, and S. Isoda, J. Microsc. **236**, 128 (2009).

[43] A. Tanaka and T. Jo, J. Phys. Soc. Jpn. **63**, 2788 (1994).

[44] B. Tsukerblat, in *Group Theory in Chemistry and Spectroscopy*, edited by D. Craig and R. McWeeny (Academic, London, 1994).

[45] E. Stavitski and F. M. F. de Groot, Micron **41**, 687 (2010).

[46] F. M. F. de Groot, J. C. Fuggle, B. T. Thole, and G. A. Sawatzky, Phys. Rev. B **41**, 928 (1990).